Analytical and Bioanalytical Chemistry (2024) 416:6317–6331
https://doi.org/10.1007/s00216-024-05518-z

RESEARCH PAPER

Extraction of redox extracellular vesicles using exclusion-based sample preparation

Mohammad Dehghan Banadaki[1] · Nicole G. Rummel[2,3] · Spencer Backus[1] · David Allan Butterfield[2,3] · Daret K. St. Clair[3,4] · James M. Campbell[3,4] · Weixiong Zhong[5] · Kristy Mayer[5] · Scott M. Berry[1] · Luksana Chaiswing[3,4]

Received: 17 May 2024 / Revised: 18 August 2024 / Accepted: 21 August 2024 / Published online: 7 September 2024

Abstract

Studying specific subpopulations of cancer-derived extracellular vesicles (EVs) could help reveal their role in cancer progression. In cancer, an increase in reactive oxygen species (ROS) happens which results in lipid peroxidation with a major product of 4-hydroxynonenal (HNE). Adduction by HNE causes alteration to the structure of proteins, leading to loss of function. Blebbing of EVs carrying these HNE-adducted proteins as a cargo or carrying HNE-adducted on EV membrane are methods for clearing these molecules by the cells. We have referred to these EVs as Redox EVs. Here, we utilize a surface tension-mediated extraction process, termed exclusion-based sample preparation (ESP), for the rapid and efficient isolation of intact Redox EVs, from a mixed population of EVs derived from human glioblastoma cell line LN18. After optimizing different parameters, two populations of EVs were analyzed, those isolated from the sample (Redox EVs) and those remaining in the original sample (Remaining EVs). Electron microscopic imaging was used to confirm the presence of HNE adducts on the outer leaflet of Redox EVs. Moreover, the population of HNE-adducted Redox EVs shows significantly different characteristics to those of Remaining EVs including smaller size EVs and a more negative zeta potential EVs. We further treated glioblastoma cells (LN18), radiation-resistant glioblastoma cells (RR-LN18), and normal human astrocytes (NHA) with both Remaining and Redox EV populations. Our results indicate that Redox EVs promote the growth of glioblastoma cells, likely through the production of H_2O_2, and cause injury to normal astrocytes. In contrast, Remaining EVs have minimal impact on the viability of both glioblastoma cells and NHA cells. Thus, isolating a subpopulation of EVs employing ESP-based immunoaffinity could pave the way for a deeper mechanistic understanding of how subtypes of EVs, such as those containing HNE-adducted proteins, induce biological changes in the cells that take up these EVs.

Keywords Extracellular vesicles · Redox EVs · 4-Hydroxynonenal (HNE) · EV isolation · EV purification · Immunoaffinity

Introduction

Cancer-derived EVs have potential to be therapeutic, promote aggression, and/or serve as disease biomarkers [1]. For example, it was recently demonstrated that EVs that were derived from radiation treatment contained mitochondria, and these radiation-derived EVs could contribute to prostate cancer regrowth after radiation [2]. EVs that are derived from tumor cells are capable of communicating with the cells in the tumor microenvironment, potentially promoting progression and immunosuppression [3]. Studying specific subsets of EV populations would help provide evidence for their role in cancer progression. EVs vary in size, cargo, and mode of biogenesis causing their characterization to be complex. Various isolation methods have been developed for the purification of the different types of EVs.

Mohammad Dehghan Banadaki and Nicole G. Rummel contributed equally to this work.

✉ Scott M. Berry
scott.berry@uky.edu

✉ Luksana Chaiswing
l.chaiswing@uky.edu

[1] Department of Mechanical Engineering, University of Kentucky, Lexington, KY 40506, USA

[2] Department of Chemistry, University of Kentucky, Lexington, KY 40506, USA

[3] Markey Cancer Center, University of Kentucky, Lexington, KY 40536, USA

[4] Department of Toxicology and Cancer Biology, University of Kentucky, Lexington, KY 40536, USA

[5] Department of Pathology and Laboratory Medicine, University of Wisconsin-Madison, Madison, WI 53706, USA

EV isolation techniques can be broadly categorized into four different methods: ultracentrifugation, density gradient separation, polymer precipitation, and immunoaffinity and microfluidic methods [4]. There has been some promising work in combining microfluidics technique with size or density differentiation [5]. Except for immunoaffinity, all the other methods are based on either size or density of the EVs. As a limitation, size/density-based methods are not useful for biomarker-specific isolation of EV subpopulations and might result in a co-purification of other molecules, such as lipoproteins, which could complicate the downstream analysis of EVs [6]. On the other hand, immunoaffinity methods use antibodies to separate EVs based on their known surface markers such as tetraspanins (CD9, CD63, CD81) [7], which results in a more specific subpopulation and purified EVs. When purification of a specific subpopulation of EVs is desired, a combination of size/density methods and immunoaffinity can be used. Sharma *et al*. used a combination of techniques to isolate melanoma related EVs from a background of EVs. In brief, they used a preliminary size-exclusion chromatography to purify EVs from the plasma of patients and then used monoclonal antibodies specific to the CSPG4 epitope (expressed on melanoma cells) to purify melanoma-related EVs [8]. Antibody-based assays can also be used to detect a subpopulation of EVs directly. In a work by Yoshioka *et al*., circulating cancer-derived EVs were directly identified in the blood of colorectal cancer patients using the CD147 antigen that is specific to cancer-related EVs [9]. Additionally, magnetic immunoaffinity techniques have been applied inside of a microfluidic device to increase binding efficiency [10, 11]. While immunoaffinity methods can isolate subpopulations of EVs, their progress is hampered because of their lengthy and expensive protocols. Moreover, many of these methods use irreversible capture mechanisms to purify sub-populations of EVs. While this might not pose a problem for certain downstream analyses, intact sub-populations of EVs are crucial for other applications [12]. As a result, there is an unmet need to produce a simple, fast, and cost-effective immunoaffinity-based method that can purify intact subpopulations of EVs [13]. Our aim is to isolate a subpopulation of EVs related to lipid peroxidation and measure the effect of these EVs on different cell types.

Oxidative stress is a phenomenon that is caused by the imbalance between the production of reactive oxygen species (ROS) and the cell's ability to detoxify them from the system [14]. ROS vary in mechanisms of generation, and there are a variety of species defined as ROS. Superoxide, hydrogen peroxide (H_2O_2), hydroxyl radicals, and singlet oxygen are among the most common ROS [15]. ROS production occurs through enzymatic and nonenzymatic reactions. Primary ROS, if not kept in balance, can also lead to ROS. Lipid peroxidation (LPO) is a common mechanism for the production of reactive aldehydes, with the initial step of the process being abstraction of a labile allylic hydrogen from a polyunsaturated fatty acid [16]. One product of lipid peroxidation through the nonenzymatic pathway is 4-hydroxynonenal (HNE). HNE is part of different cellular signaling pathways and contributes to biological functions including stimulation and inhibition of enzymes [17]. Adduction by HNE causes, due to high concentrations of HNE, changes the protein conformation and often leads to loss of function [18–20]. Oxidative stress-induced HNE formation has been strongly tied to the formation of cancer and other diseases [21, 22]. One observed mechanism to eliminate the damage is the production of extracellular vesicles (EV). The lipid bilayers of cell membranes are rich in polyunsaturated fatty acids and therefore cell membranes are rich in labile allylic H-atoms on unsaturated acyl chains of phospholipids, the initiation sites for LPO. We demonstrated that one of the HNE-preferred target proteins on the cell membrane is flippase [23], an ATP-dependent enzyme which translocates phosphatidylserine (PtdSer) from the outer leaflet back to the inner leaflet. When HNE adductes Cys of flippase, a conformational change of flippase occurs and leads to inactivation of flippase [24]. Impairing of flippase results in PtdSer flip to outer bilayer leaflet and when an overwhelming amount of PtdSer is on the outer leaflet, it contributes to the shedding of EVs, microvesicles [25].

We have recently identified extracellular entities termed redox-extracellular vesicles (Redox EVs), EVs containing HNE-adducted proteins that can be detected by liquid biopsy of the blood [26]. Given the significance of HNE-adducted proteins in causing cellular damage and the crucial role of EVs in cancer and neuro-associated diseases [21, 27, 28], our objective in this study is to isolate Redox EVs. The ability to detect EVs through liquid biopsy demonstrates their clinical diagnostic potential in conditions including radiation-induced brain injury or chemotherapy-induced cognitive impairments [26, 29, 30] as well as hard-to-diagnose cancers such as glioblastoma (GBM), a deadly cancer that seriously reduces quality of life due to wide-ranging neurologic impairment. GBM is also among the most challenging cancers to treat. Several factors contribute to the challenge, including the lack of a sensitive non-invasive method of early detection, the diffuse infiltrative nature of GBM, and tumor spatiotemporal heterogeneity.

Despite the abundant amount of EVs in GBM serum [31–33], isolation of subpopulation of EVs still need to be further developed. Precipitation methods have been reported to negatively impact the biological activity of isolated EVs and are prone to co-precipitating non-EV materials, such as protein aggregates, polymeric materials, other vesicles, and lipoparticles, which can lead to contamination [34, 35]. While flow cytometry can be used to isolate rare EV subpopulations from a heterogeneous population [36], identifying,

sorting, and studying distinct subsets of EVs requires highly specialized and costly equipment, such as nanoscale Fluorescence Analysis and Cytometric Sorting (nanoFACS). This is because the majority of EVs fall below the minimum detection threshold for even the most sensitive flow cytometers [36]. Moreover, the recovery rate of these methods is moderately low, considering the high volume of original samples used. Consequently, isolating any specific EV subpopulation, including Redox EVs, through immunoprecipitation or cell sorting flow cytometry is a time-consuming and labor-intensive process that demands large sample volumes and access to expensive instrumentation. Because of the caveats of the aforementioned EV isolation techniques, we have turned to a platform called exclusion-based sample preparation (ESP), which has previously been utilized to efficiently isolate small quantities of nucleic acids, proteins, and whole cells, but not EVs [37–40]. Recently, ESP has been successful in simplifying the extraction of SARS-CoV-2 RNA from wastewater samples [41–43]. Briefly, ESP utilizes hydrophobic surfaces and reagent surface tension to create several air/aqueous phase interfaces along a singular linear path. With this configuration, paramagnetic particle (PMP)-bound analytes can be drawn through multiple aqueous reagents (e.g., washing buffers) using a single linear motion. This results in a simple and rapid isolation process that has been shown to produce much higher yields than traditional immunoaffinity isolation protocols [37, 44, 45]. The process can be further improved via automation of ESP, which was recently introduced [46]. In summary, the objective of this study was to determine, for the first time, if ESP technology could be utilized to isolate Redox EVs. Additionally, the Redox EVs are characterized, and their impact on cells is examined. Part of this work has been previously presented as a conference poster presentation.[1]

Material and methods

Cell lines

The human glioblastoma cell line, LN18, was obtained and authenticated by ATCC (Catalog Number CRL-2610). Radiation resistant LN18 cells (RR-LN18) were developed from LN18 cells by exposing them to 2 Gy radiation, 5 days/week, until obtained a total of 60 Gy. RR-LN18 cells were authenticated using target short tandem repeat (STR) markers provided by ATCC cell authentication service. Normal human astrocyte (NHA) cells were obtained from Lonza (Catalog Number CC-2565). LN18-cells were adherent in culture and were maintained in T75 tissue culture flasks (Corning, AZ) in complete medium (RPMI-1640 media supplemented with 10% FBS, 5% penicillin streptomycin, 5% L-glutamine, 5% Sodium Pyruvate, and 5% HEPES buffer). Cells were grown in a humidified atmosphere at 5% CO2 in air at 37°C. Cells were detached with Trypsin-EDTA. LN18 cells were seeded in complete media and allowed to adhere overnight. Once adhered to the flask surface, the media was removed, and the cells were washed with 1X PBS. Complete media with ExoFree FBS (System Biosciences, CA) was added to the cells and they were subjected to 6 Gy radiation, to promote production of HNE. The cells were then incubated for 48 h. This was followed by media collection and filtration of the media through a 0.8 µm Acrodisc filter to remove any of the larger cell debris. EVs were then isolated from the media directly (as described in 2.2) and analyzed for the number of EVs produced.

EV purification

Cells were seeded in complete medium at 8×10^5 cells/ml, 15 ml/plate in a 15-cm culture dish and allowed to adhere overnight. Cells were washed twice with PBS (Thermo Fisher Scientific, MA) and media was replaced with complete media containing 10% ExoFree FBS (System Biosciences, CA). Cells were then treated with 6 Gy radiation and incubated for 48 h. Media was removed from the cells and filtered using a 0.8 um Acrodisc filter. Total extracellular vesicles were isolated via the Qiagen ExoEasy Maxi Kit (Germantown, MD, USA) per the protocol provided. Extracellular vesicles were eluted from the filter using 1 ml of elution buffer. EVs were concentrated using Amicon Ultra-0.5 mL centrifugal filters for DNA and protein purification and concentration to 60 µL per 15 ml of media. EVs were stored at −80°C until further use.

Isolation of Redox EVs via ESP

Redox EVs were isolated from total EVs (derived from step 2.2) using ESP, which utilizes surface tension to simplify the isolation of paramagnetic particle (PMP)-bound analyte from a complex sample. Specifically, anti-4Hydroxynonenal (4HNE) antibody (ab46545, Abcam) conjugated to Dynabeads Protein G (10007, Thermo Fisher) was used as the capture mechanism to isolate Redox EVs from a background of EVs. These PMPs are 2.8 μm superparamagnetic with recombinant Protein G (~17 kDa) coupled to their surface. Prior to use, the Dynabeads (with a stock concentration of 30mg/ml) were washed three times by placing the tube on a MagJET Separation Rack (MR02, Thermo Fisher), removing the supernatant, and resuspending the Dynabeads in Ab

[1] Dehghan Banadaki M., Rummel N. G., Backus S., Butterfield A.D., St. Clair D.K., Campbell J.M., Zhong W., Mayer K., Berry S.M., Chaiswing L., Extraction of redox extracellular vesicles using exclusion-based samples preparation. SfRBM 2023 & SFRRI 21st Biennial Meeting, Poster Presentation, Punta del Este, Uruguay, 2023.

Binding & Washing Buffer (10007D, Thermo Fisher). Isolation of Redox EVs from the sample requires conjugation of anti-HNE antibody to beads. To determine the concentration of antibody that would allow for optimal isolation of Redox EVs, three different concentrations were chosen, 0.2 µg antibody per 1 mg bead, 1.0 µg antibody per 1 mg bead, and 5.0 µg antibody per 1 mg bead. We compared the isolated EVs from these three antibody concentrations using various metrics such as total EVs concentrations, EVs size, HNE adducted protein profile, total flotillin-1, and albumin contamination. The optimal antibody concentrations were identified and used in the final experiments. The anti-4-HNE antibody (with a stock concentration of 0.71mg/ml) was mixed at different concentrations with PBS to make a 1:10 dilutions, and this was mixed with the PMPs and additional Ab Binding & Washing buffer to increase the volume to 200 µL. This volume was necessary to ensure complete mixing via 20 min of tumbling on a rotator at 20 rpm (i.e., smaller volumes would remain in the tip of the tube due to the surface tension of the solution). Subsequently, the same wash process was done three times using Ab Binding & Washing Buffer to remove all the unbound antibodies. After taking out the supernatant from the antibody-PMP mixture, the EV sample was added to the PMPs, and PBS was added to reach the total volume to 500 µL. The tubes were put on the rotator at 20 rpm for another 20 min at room temperature to promote binding between the antibodies and EVs. After incubation, the entire volume was loaded into the input well of ESP plate and washed three times in PBS (see next section for details of the ESP process). Following ESP, the PMPs were incubated with 30 µL of elution buffer from the Immunoprecipitation Kit (10007D, Thermo Fisher) for 5 min at room temperature, and the supernatant was collected for downstream analysis. Additionally, the contents of the input and wash wells were collected to analyze fractions not selected by the ESP process.

ESP operation

To perform ESP selection of the EVs, the Extractman device (22100000, Gilson) was utilized. In brief, the Extractman is a platform that uses two movable magnets (one above the sample plate and one below) to rapidly move PMPs (and associated analytes) through a series of buffers. As the Extractman head slides over wells on the extraction plates (22100008, Gilson), the upper magnets immobilize the PMPs on a hydrophobic strip (22100007, Gilson), and when the head slides over to the next well, the lower magnet deflects the upper magnet upward, making the dominant magnetic force downward, which then pulls the PMPs from the strip into the wash well (Fig. 1). The device and plate allow simultaneous processing of four samples.

Size and concentration measurement of Redox EVs

The size and concentration of Redox EVs were measured using the ZetaView NTA nanoparticle tracking device. EVs were diluted to a final concentration of 1:1000 in 1% PBS in ultrapure H_2O. 1 mL aliquots were injected into the instrument. The sample was measured for size and concentration in scatter mode based on Brownian motion (520 nm laser) (sensitivity 80, shutter 80, brightness 15, min area 15, max area 1000). The resulting videos were analyzed using the ZetaView® Software version. With laser wavelength 520

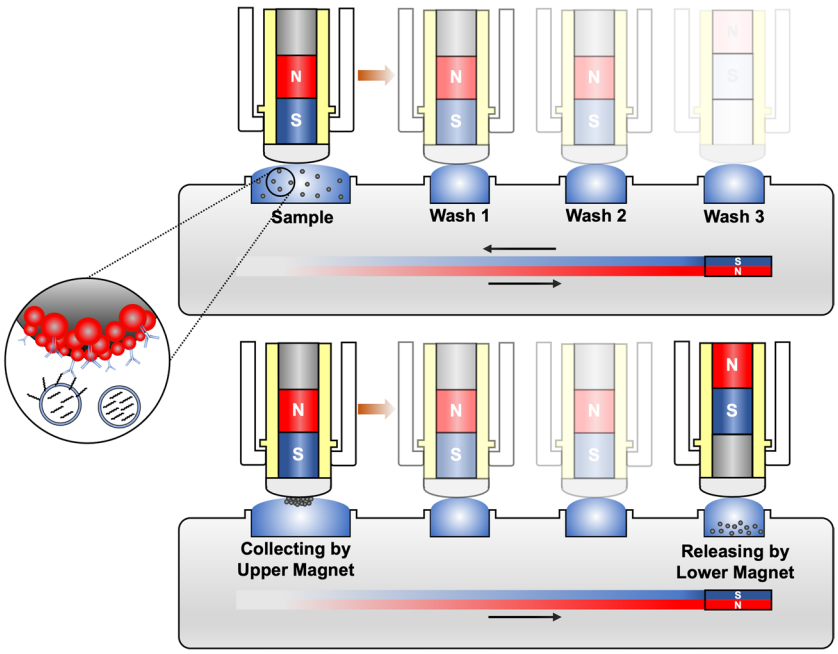

Fig. 1 Schematic of exclusion-based sample preparation (ESP) technology for isolation of HNE-adducted Redox EVs

nm, focal wave length 75 mm, and focal thickness of 25 µm, the camera looks at an area of 640×480 pixels, which corresponds to 460×345 µm. It should be noted that the photo from CMOS camera of NTA instrument does not directly capture the physical size of particles. As a result, the brightness observed in the NTA images is not directly proportional to the size of the particles but rather reflects the number of particles in a given view. The camera records a one-dimensional projection of the scattered light, which does not account for the *z*-dimension or the actual spatial distribution of particles in the sample. In the experimental setup, particles are visualized using a 520 nm laser, and their movement is tracked using a CMOS camera positioned at a 90° angle. The photo shows scattered light from particles, with their apparent size being inferred through analysis of their Brownian motion. The size of each particle is determined by analyzing the Brownian motion captured in the video from l3 view/angles. The movement of particles, driven by interactions with surrounding molecules, is characterized by the diffusion coefficient. This relationship, described by Albert Einstein, is utilized in the Stokes-Einstein equation to calculate the particle diameter. Therefore, the size measurements in NTA are derived from the dynamic behavior of particles, not from direct dimensional imaging.

Protein analysis of Redox EVs

EVs were lysed using 5x EV lysis buffer (5x RIPA, 5x Protease Inhibitors, 5x EDTA, Cell Biolabs, Catalog number AKR-190). 5x EV lysis buffer was added to EVs to achieve a final concentration of 1x EV lysis buffer. Samples were sonicated for 15 s and placed on ice for 1 min for a total of three times. Samples sat on ice for an additional 30 min. The Jess^{TM} Simple Western automated nano-immunoassay system (ProteinSimple, Bio-Techne) was used to evaluate cell lysate and EV lysate samples [47, 48]. Samples were processed according to the manufacturer's standard method for the 12–230 kDa Jess Separation Module (SM-W002), the Anti-Rabbit Detection Module (DM-001), and the Protein Normalization Module (SM-FL001, DM-PN02). The compass simple western software (version 6.0.0) was used for the automatic calculation of peak area (chemiluminescence intensity) and signal/noise ratio as well as to capture the digital image of the capillary chemiluminescence. The protein levels of Flotillin-1 and albumin were assessed, along with the levels of 4-hydroxynonenal-bound proteins. Primary antibodies were diluted to 1:20 concentrations for all samples. 1×10^8 EVs per sample were used in each well for Jess.

Electron microscopic (EM) imaging of Redox EVs

Transmission electron microscope imaging coupled with immunogold labeling were performed by our colleagues at the University of Wisconsin-Madison. EVs were fixed by combining the sample 1:1 in 2% glutaraldehyde in 0.1 M sodium phosphate pH 7.4 (10 µL sample added to 10 µL 0.1 M sodium phosphate pH 7.4, 1:2 dilution) for 30 min at room temperature. After 30 min, if further dilution was needed, a solution of 1:1 in 0.1 M sodium phosphate pH 7.4 for the 1:4 dilution (6 µL of each) was used. A total of 5 µL of fixed EVs were then placed on parafilm. A copper grid was placed on the drop for 10 min. Excess liquid was removed by blotting, washing twice for 5 min in 100 µL sterile water, and then blotted again to remove water. Grids were incubated in 50–100 µL drops of anti 4HNE-adducted antibody (ab48506, Abcam) diluted 1:25 in PBS containing 0.1% BSA and stored at 4 °C overnight. Grids were transferred to drops of secondary antibody conjugated to 10 nm gold particles diluted 1:100 in PBS containing 0.1% BSA and incubated for 1 h. The final product was stained in 30 µL 1.5% uranyl acetate in water for 45 s to 1 min, blotted, and then used to perform the assay. Grids were photographed with a Hitachi H-600 electron microscope. EVs from normal mouse serum (sc-45051, Santa Cruz Animal Health) was used as non-redox controls for the EM imaging.

Treatment with Redox EVs and cell viability of LN18 glioblastoma and normal human astrocyte cell lines

LN18 and radiation resistance LN18 (RR-LN18, cells that survived clinical relevance dose of radiation 60 Gy) and normal human astrocyte (NHA cells) were seeded separately at 2×10^3 cells per well on a 96 well plate in complete media and allowed to adhere overnight. Media was aspirated and the cells were rinsed with 1x PBS and fresh media was added to the wells. Remaining EVs (non-Redox EVs) and Redox EVs were added to the wells at a total amount of 5×10^6 EVs per well. Cells were incubated for 48 h at 37°C. The PrestoBlue cell viability assay (Thermo Fisher Scientific, MA) was performed to measure the viability of cells after EV treatment. Absorbance measurements were taken at 560 nm and 600 nm with a Spectramax 384 plus Microplate Reader (Molecular Devices, San Jose, CA, USA); the 600 nm values were used for normalization. To determine cell viability of LN18 cells, RR-LN18 cells, and NHA cells after EV treatments with or without the presence of polyethylene glycol-catalase (PEG-CAT), an enzyme that scavenges intracellular H_2O_2, 5×10^4 cells were seeded per well on a 24 well plate in complete media and allowed to adhere overnight. Media was aspirated and the cells were rinsed with 1x PBS, and fresh media was added to the wells. PEG-CAT (500 units, Nanocs Inc., NY) were added to the cells for 24 h. Remaining EVs and Redox EVs were then added to the cells at a total amount of 5×10^6 EVs per well. After 48 h treatment of EVs, cells were then harvested with Trypsin-EDTA, neutralized with media contained FBS, centrifuged at 300 g, 5 min,

4°C (to remove excess Trypsin-EDTA), and suspended in 1 mL fresh media. To perform a cell count using Trypan blue, 10 µL of the cell suspension were mixed with 10 µL of 0.4% Trypan blue solution (Thermo Fisher, MO) and incubated for 2–3 min at room temperature. Stained cell mixture was loaded into a hemocytometer; viable cells (unstained) and non-viable cells (stained) were counted in designated hemocytometer grid areas. Total cell concentration was calculated by multiplying the average count per grid by the dilution factor and the hemocytometer's volume factor.

Measurement of ROS production in RR-LN18 cells and NHA cells

Cells were seeded in complete medium at 50,000 cells/well in 24 well black microculture plates (with glass bottom) and allowed to adhere overnight. The cells were then washed twice with PBS, and fresh complete media ((-) phenol red) was added to the wells. Remaining EVs and Redox EVs were added to the wells at a total amount of 5×10^6 EVs per well. Cells were incubated for 48 h at 37°C. Media was removed from the wells and placed into a new 96 well black microculture plate. Amplex Red Assay Kit (Invitrogen) was used, and the Amplex red solution was prepared in accordance with the protocol of the kit. A 1:1 ratio of Amplex red solution was added to the media and incubated for 1 h. The fluorescence relative unit was measure at excitation 570nm/emission 590 nm with BioTek Cytation 5 Cell Imaging Multimode Reader. To prepare H_2O_2 standard curve, serial dilutions of H_2O_2 (0.0675, 0.125, 0.25, 0.5, 0.75, and 1 uM) were prepared from a stock solution of H_2O_2 (30 mM) and added to a 96-well black plate in triplicate. The fluorescence signal was plotted against H_2O_2 concentration to generate the standard curve. The resulting linear relationship demonstrates the assay's sensitivity and accuracy for detecting and quantifying H_2O_2. Data points represent the mean ± standard deviation of triplicate measurements (Figure S3).

Statistical analysis

All the experiments are performed in four replicates to account for the heterogeneity between replicates. One-way ANOVA or Student's *t*-test were used to analyze the mean difference across groups and between groups, respectively. Multiple pairwise comparisons between groups were adjusted using LSD test or Turkey test. Statistical analyses were performed using GraphPad Prism 9.1.0 (Dotmatics, Boston, MA, USA). A two-sided *P*-value of less than 0.05 was considered significant or otherwise specified at the figure legends. Data were displayed as mean + standard error. Data analysis for cell viability were displayed as fold change compared with control (buffer).

Results and discussion

Radiation enhances EV production in LN18 glioblastoma cells

Compared with normal cells, cancer cells are known to produce higher levels of EVs [49]. The increased levels of oxidative stress and redox state within the cells have been shown to lead to increased production of EVs [50]. Radiation is a common treatment for cancer in conjunction with chemotherapy. Radiation leads to cellular damage at multiple levels and is known to induce ROS production within cells [51, 52]. Through the use of radiation on cancer cells (e.g., LN18 glioblastoma cells), increased ROS levels and increased EV production can occur. As shown in Fig. 2A, the number of EVs present in the no treatment control are visibly less than those present after 6 Gy radiation. The ZetaView NTA instrument uses light scattering to efficiently count and measure the sizes of the EVs. Histogram graph represent the distribution of EVs size and concentration which are demonstrated in Fig. 2B. After analyzing the total number of EVs within the sample, there is a significant increase in the number of EVs but smaller in size after 6 Gy radiation (Fig. 2C–D). The EVs produced after radiation treatment were used for the following experiments involving the ESP technique for the isolation of Redox EVs.

EVs isolated directly from media demonstrate the presence of Redox EVs

In order to assess the sensitivity of the ESP technology, Redox EVs were isolated from cell culture media. LN18 cells were seeded at 8.0×10^5 cells/mL in 15 mL of complete media and allowed to adhere overnight. The following day, the media was aspirated, and the cells rinsed with 1X PBS. Complete media with exosome-free FBS was added to the cells. The cells were subjected to 6 Gy radiation and allowed to incubate. After 48 h, cells were removed from the incubator, and the media was removed and filtered through a 0.8 um Acrodisc Filter to ensure removal of large debris. The media was concentrated using Amicon Ultra-0.5 mL centrifugal filters to half the original volume. Media was then subject to the ESP platform for further Redox EVs isolation. The EVs isolated using the ESP technology and those remaining were assessed for size and zeta potential. Studies on the number of EVs revealed that Redox EVs are only a small fraction of the total EVs (Figure S1). The difference in sizes of the two populations does not indicate the presence of exosomes (<100 nm) in either of the populations. However, EVs in

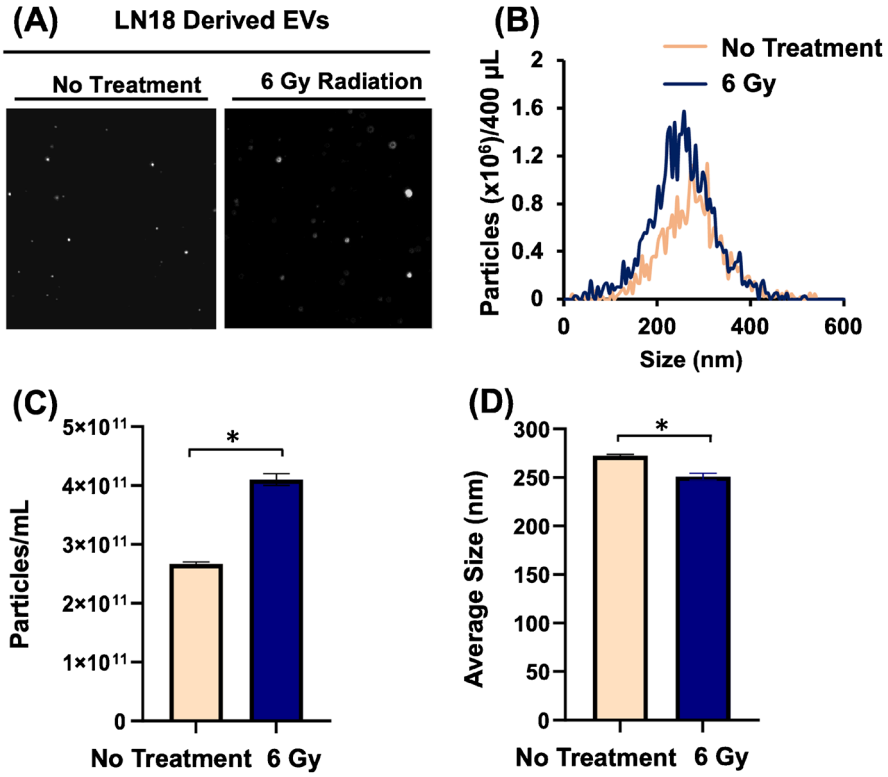

Fig. 2 LN18 cells were plated at 1.2×10^7 cells in a 15-cm dish. Twenty-four hours after plating, one plate was radiated at 6 Gy. Both plates incubated for 48 h. Media was collected and filtered to remove large debris. EVs were isolated (as described in the "EV purification" section), and the number of EVs were counted using NTA. Radiation at 6 Gy induces EV production within LN18 cells. **A** Photograph of EV particles (white dots) from NTA. **B** Size distribution of EV. **C** EV concentration. **D** Size of EVs. (*$P<0.05$)

the ESP-selected fraction (termed the Redox EV fraction) have a smaller size compared with the EVs remaining following ESP selection (Fig. 3A). The smaller size may be attributed to their increased negative potential which was observed via measurement of the zeta potential (Fig. 3B).

There are various mechanisms of production for EVs within the cell, one of which involves the presence of phosphatidylserine (PtdSer) on the outer leaflet of the cell [53]. Under physiological conditions, the presence of PtdSer on the outer leaflet may induce apoptosis [54]. However, the survival of cancer cells depends on the ability to inhibit this pathway. PtdSer is a negatively charged phospholipid typically seen on the inner leaflet of the cell. The presence on the outer leaflet and the associated increased negative charge causes a pucker in the cell membrane initiating EV blebbing. Redox EVs are prone to PtdSer on the outer leaflet due to the increased oxidative damage within the cell and therefore would have a higher negative potential. Figure 3B indicates the significant change in zeta potential between the two populations with the Redox EVs exhibiting a higher negative potential compared with the Remaining EVs. Not only do their size and zeta potential differ in the two populations, but the HNE-adducted protein profile within the EVs also differs. Redox EVs show a limited number of proteins with HNE adduction compared to the EVs remaining (Fig. 3C).

Optimization of antibody concentration for efficient isolation of Redox EVs

Total EVs were purified directly from filtered conditioned media and subjected to ESP isolation of Redox EVs. The concentration and size of EVs captured by the antibody-conjugated beads was measured using the ZetaView NTA nanoparticle tracking instrument. The amount of EVs captured by the beads was highest at the 0.2 µg antibody/mg bead (Fig. 4A). The concentration 5.0 µg antibody/mg bead captured the lowest amount of EVs. This drop-in performance at high antibody concentration may be due to steric hindrance, where an over-abundance of antibody binding domains act to occlude one another. Size of the EVs captured is lowest using the 0.2 µg antibody/mg bead (Fig. 4B). Redox EVs with 0.2 µg antibody/mg bead have a smallest size compared to 0.5 µg antibody/mg bead. It should be noted that from a biological perspective, and in accordance with the MISEV2024 guidelines [55], the size range of EVs between 100 and 300 nm does not result in significant differences in their biological functions or activities. This size range is commonly observed for EVs and includes both exosomes and microvesicles, which are known to overlap in size distribution and share many functional characteristics.

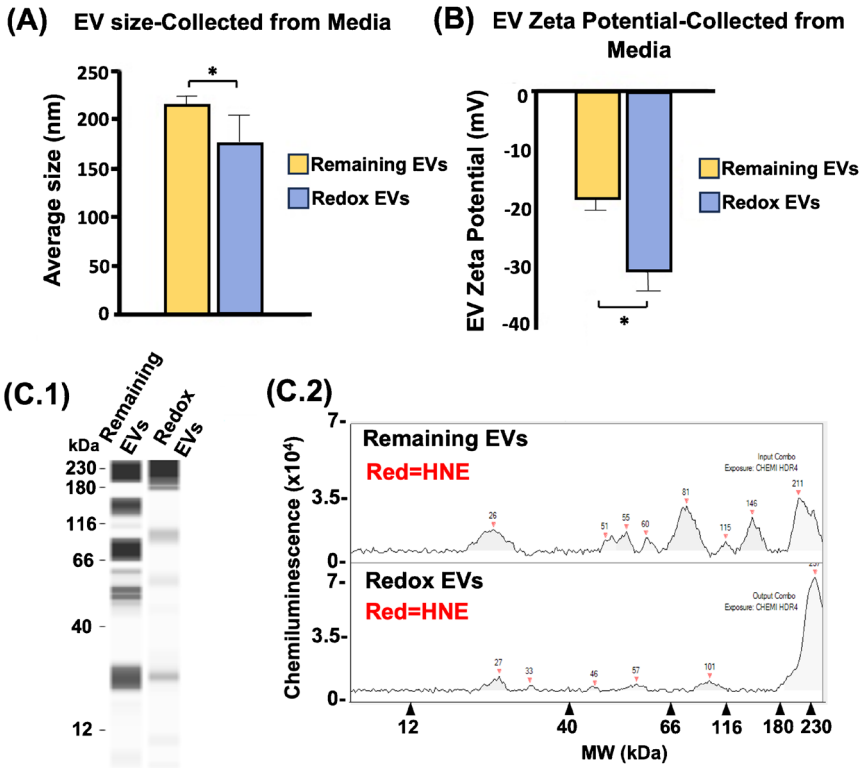

Fig. 3 Initial isolation of Redox EVs directly from media. The term "Remaining EVs" refers to EVs that are still present in the input sample after the process of Redox EVs isolation. **A** EVs size comparison. (*P<0.05), **B** EVs zeta potential comparison. (*P<0.05), **C** HNE-adducted protein profile compared between the Remaining and Redox EVs. C.1 = Lane-view data of HNE band. C.2 = Electropherogram data of HNE peaks (red arrow) at each molecular weight

Redox EVs are defined by EVs that contain HNE-adducted proteins as their cargo or on EVs surface. Here in, we measured the level of HNE-adducted proteins using the Jess ProteinSimple western blot analysis. The highest presence of HNE-adducted proteins was observed with the use of 1.0 µg antibody/mg bead compared with the other two concentrations (Fig. 4C). Albumin contamination can affect the quantification and functional analysis of EVs, and therefore, the amount of albumin contamination was measured. Albumin concentration was measured via the Jess ProteinSimple western blot analysis. Albumin contamination is low in all cases and lowest using 1.0 µg antibody/mg bead (Fig. 4D) compared with the other two concentrations. Flotillin-1 is used as an EV marker (for both Redox EVs and Remaining EVs) and was measured for each concentration. Each concentration contains detectible levels of flotillin-1, and 0.2 µg antibody/mg bead shows the strongest signal for flotillin-1 (Fig. 4E and F).

Washing steps facilitate control of albumin contamination in samples

To further determine which concentration of Ab conjugated to the streptavidin beads was most appropriate for isolating HNE-adducted Redox EVs, the washing steps of the isolation process were analyzed to monitor loss of EVs and albumin contamination. Washing steps were concentrated using Amicon Ultra-0.5 mL centrifugal filters at 14,000 g at 30-min intervals until the final volume ranged from 50 to 60 µL. The concentration and size of EVs in the washing steps was measured via ZetaView NTA, and the videos were analyzed using the ZetaView software. Washing steps contained no quantitative number of EVs as represented by the qualitative view of the ZetaView NTA in Fig. 5A. Washing steps were analyzed for the amount of HNE and albumin present in the sample using Simple Western Jess and compared with the HNE and albumin present in the isolated HNE-adducted Redox EV sample. The same volume of sample was used to compare the wash step to the isolated sample. The albumin contamination in captured EVs compared with the wash buffer is shown in Fig. 5B. The 1.0 µg of antibody/mg bead shows one of the lowest albumin contaminations in the EVs and highest in the wash step. As shown in Figure S2, the albumin contamination is much lower in the Redox EVs than the Remaining EVs, proving that ESP is effective in removing the contamination. As shown in Fig. 5C, while HNE is also present in the washing steps, the loss of HNE at wash steps decreases with lowering the antibody concentration. A higher amount of HNE can be found in the washing step with the use of 1.0 µg of antibody/mg bead, which can be explained by the avidity of immobilized antibody, and therefore surface crowding [56]. Since flotillin-1 is a marker for both Redox EVs and Remaining EVs, it might be found in the washing step. As shown in Fig. 5D and E, the use of 1.0

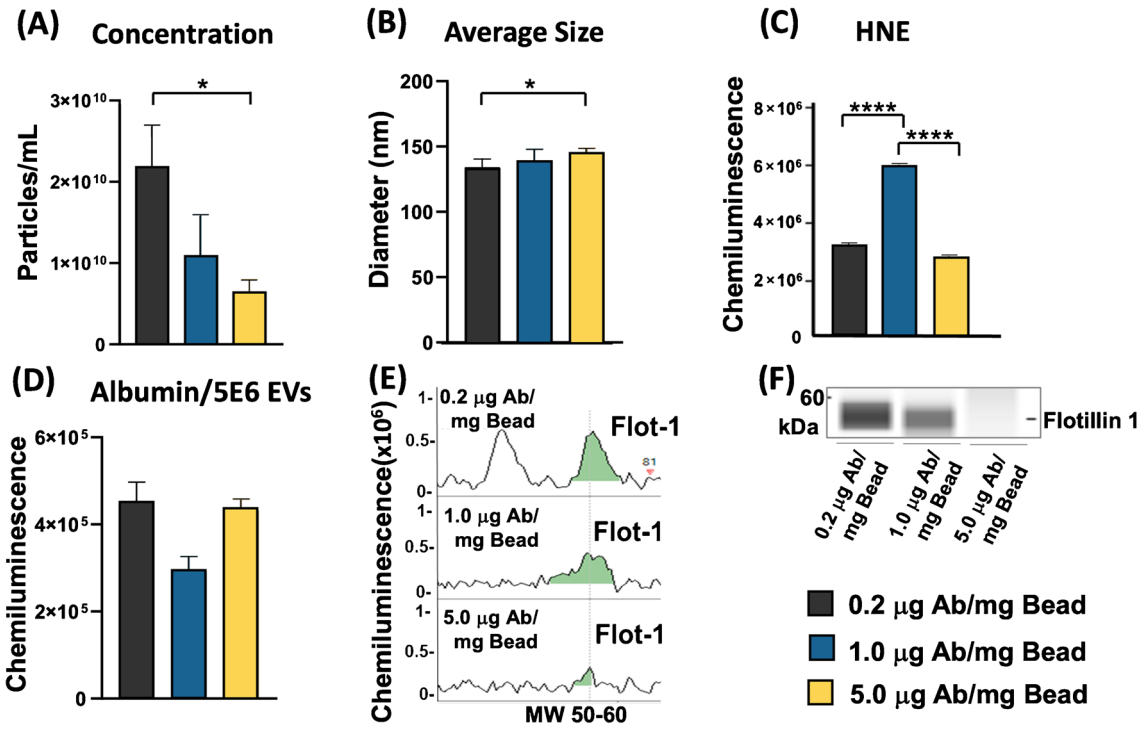

Fig. 4 Optimization of antibody concentration for efficient isolation of Redox EVs. **A** Concentration of Redox EVs increased with decreasing concentration of antibody bound to the beads. (**P*<0.05). **B** Average size of EVs decreases with decrease in the antibody concentration bound to the beads (**P*<0.05). **C** HNE concentrations are higher in the EV with the use of 1.0 µg of antibody per mg of bead. (*****P*<0.0001). **D** Albumin contamination remains low in either of the concentrations of antibody. **E** Flotillin-1 (Flot-1) was present mostly with the use of 0.2 µg of Antibody per mg of beads. Electropherogram data (area under the curve, green) and **F** lane-view data represent level of Flot-1

µg of antibody/mg bead displays flotillin-1 in the washing step which also potentially indicates a loss of HNE-adducted Redox EVs in the washing step. Flotillin-1 is not present in the washing steps using 0.2 µg of antibody and 5.0 µg of antibody. The minor shift of Flot-1 in lane view (Fig. 5E) is a result of how the Compass software converts Gaussian peak fits into lane views option. This software, while useful for visualizing lane data, is not always perfect in aligning bands, especially when dealing with peaks that have a broad width at the base. This misalignment is a visual artifact of the software and does not affect the actual data which are calculated from the area under the curve (green) of chemiluminescence signal.

ESP-isolated sample contains Redox EVs

Comparing the results from the first round of optimization and the analysis of the washing steps (Table 1), the concentration of 0.2 µg of Ab per mg of beads was chosen for further testing. EVs were isolated using 0.2 µg of Ab per mg of beads, and 1.0 mg of beads were used. The isolated HNE-adducted Redox EVs were compared with the EVs that remained in the original sample labeled as Remaining EV. Zeta potential and size were measured via the ZetaView NTA, and the videos were analyzed using the ZetaView Software. HNE-adducted Redox EVs had a more negative zeta potential compared with the remaining EVs in the original sample (Fig. 6A) as well as having a significantly smaller size compared with the remaining EVs (Fig. 6B). Please note that the slightly differences in EV size between Figs. 3A and 6B lies in the source of the EVs and the purity of the samples analyzed. Figure 3A includes results from EVs isolated directly from conditioned media (rather than total purified EVs), which may still contain other molecules, such as lipoproteins, dead cells, and other cellular debris, while Fig. 6B shows results from purified EV population, providing a more accurate comparison between Redox EVs and Remaining EVs under optimized conditions. To confirm the presence of EVs in the Redox EVs and Remaining EVs, flotillin-1, a marker of EVs, was measured. EVs were lysed and a total of 1.0×10^8 EVs were used per well on Simple Western Jess. As shown in Fig. 6C, with the same number of EVs, levels of flotillin-1 marker are higher in Remaining EVs than Redox EVs. Interestingly, the levels of HNE-adducted proteins within the Remaining EVs are also significantly higher than the HNE-adducted protein

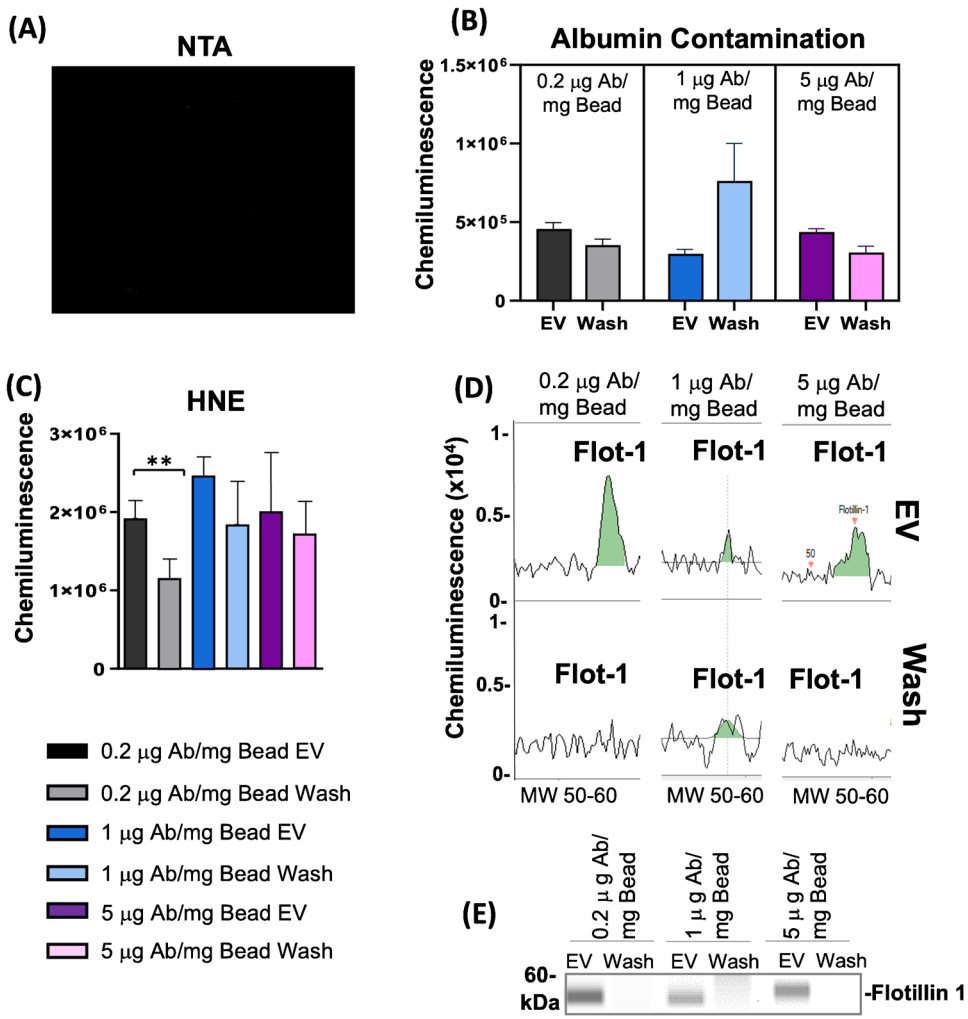

Fig. 5 Washing steps are studied to determine the amount of EVs lost and the albumin contamination. **A** NTA shows no EVs present in the washing step. The camera of NTA looks at an area of 640 × 480 pixels, which corresponds to 460 × 345 µm. **B** Using 1 µg Ab/mg bead removed albumin in the wash compared with the other two concentrations. **C** HNE levels in wash step which are significantly less in 0.2 µg Ab/mg bead (**P<0.01). **D** Electropherogram data (green, area under curve). **E** Lane-view data of flotillin-1 (EV marker), which is marker for both Redox EVs and Remaining EVs, was slightly detected in the washing steps of 1 µg Ab/mg bead

in Redox EVs (Fig. 6D). The higher amount of flotillin-1 and 4HNE-adducted proteins in Remaining EVs suggested that Remaining EVs cargo contain more proteins inside the EVs, including 4HNE-adducted proteins. Please note that ESP with anti-4HNE-adducted protein antibody only capture 4HNE-adducted proteins on the surface of intact EVs, not 4HNE adducted proteins inside the EVs. To further characterize Redox EVs, EM imaging of the isolated Redox EVs using an HNE antibody with immunogold labeling was performed. As shown in Fig. 6E, immunogold beads (10 nm) can be seen on the surface of the isolated Redox EVs compared with the mouse serum EVs and Remaining EVs which contain less HNE-adducted proteins on their outer leaflet (Fig. 6E, high magnification).

Table 1 Comparing the different conditions, 0.2 µg Ab/mg bead shows best overall Redox EV characteristics. This condition was chosen for all further testing

	Albumin	Concentration	Size	HNE
0.2 µg Ab	Low	High	Smallest	Medium
1.0 µg Ab	Lowest	Medium	Medium	High
5.0 µg Ab	Low	Low	Largest	Medium

Redox EVs promote cell viability to GBM cells but kill NHA cells via H_2O_2 production

EVs, secreted from cancer cells, containing oxidatively damaged proteins can interact with neighboring cells releasing their contents and furthering damage. Cancer cell-derived EVs have been shown to increase cell viability in neighboring cancer cells but can also have a harmful effect on normal cells [51]. Here, we validated that the Redox EVs that were isolated by the ESP technique are intact and can further be used to evaluate their function. We treated glioblastoma cells LN18, RR-LN18 (radiation resistant version of LN18) and normal human astrocytes (NHA) with both populations Remaining EVs and Redox EVs to determine their effect on viability of the cells. Each cell lines were seeded separately and treated with equal number of Remaining EVs and Redox EVs (5×10^6 EVs per well in a 96 well plate). After

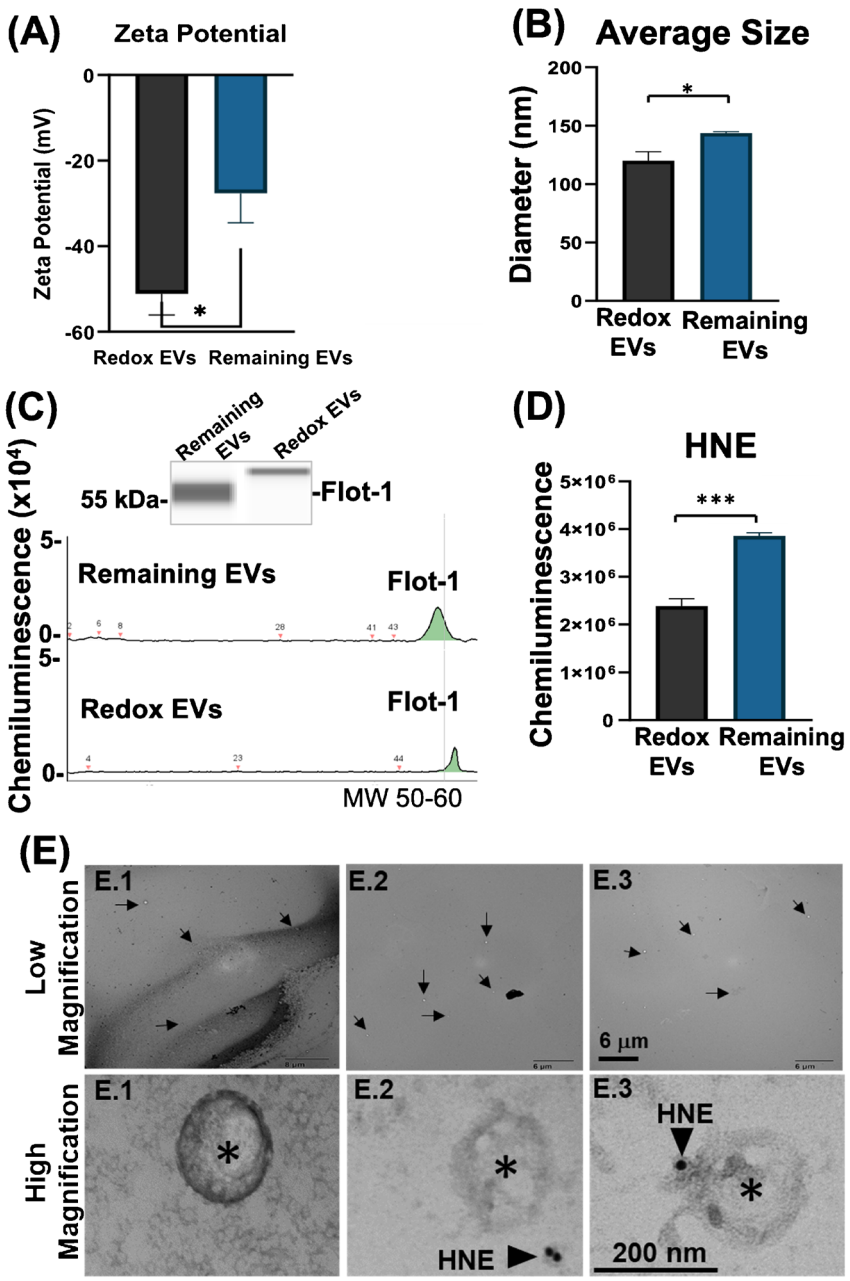

Fig. 6 Two populations of EVs were formed after using the ESP technique. Redox EVs which were isolated using HNE antibody conjugated beads and the EVs that were left behind in the isolation (Remaining EVs or non-Redox EVs). Comparing the two populations shows those that were isolated have characteristics of Redox EVs. **A** When EVs bleb from the surface, Redox EVs contain a higher amount of PtdSer on the outer leaflet giving them a more negative charge as shown by the zeta potential. (*P<0.05). **B** Average size shows that the Redox EVs are smaller than those remaining (*P<0.05). **C** Electropherogram data (green, area under the curve) and lane-view data of flotillin-1 which show slightly shift in molecular weight in the Redox EVs (possibly due to the negative charge and salt content). **D** HNE is higher in Remaining EVs, however still present in Redox EVs (***P<0.001). **E** Representative EM photograph of immunogold staining with HNE antibody. (E.1) Normal mouse serum was used as control with no gold labeling of HNE presence. (E.2) Remaining EV show labeling of HNE (arrowhead) outside the EV, whereas (E.3) Redox EV show labeling of HNE (arrow heads) present on the outer membrane of EV. Arrows = EVs at the low magnification. Star = EV at high magnification

incubation for 48 h, the cell viability was measured via the PrestoBlue cell viability assay. LN18 cells do not show a significant increase in viability after the addition of the Redox EVs (Fig. 7A), but RR-LN18 show a significant increase in viability after treatment with Redox EVs (Fig. 7B). In contrast, NHA cells show a significant decrease in viability after treatment with Redox EVs (Fig. 7C), while Remaining EVs do not have much effect on the NHA cell viability.

We conducted a detailed investigation into the mechanisms by which Redox EVs influence GBM cell viability while causing cell death in NHA cells. Prior research has demonstrated that low levels of H_2O_2 can stimulate cell proliferation through Nrf2 activation, while elevated levels of H_2O_2 lead to cell death via protein oxidations and apoptosis [57, 58]. To assess H_2O_2 production following Redox EVs treatments, we utilized Ampelx Red after 48 h. Figure 8 illustrates that Redox EVs treatment significantly increased H_2O_2 production in LN18 cells, RR-LN18 cells, and NHA cells compared with the vehicle group (EV Buffer), with RR-LN18 cells demonstrated the highest levels of H_2O_2 production (0.5 µM). Remaining EVs treatment also induced H_2O_2 production but to a lesser extent than Redox EVs treatment, in all cell types. Notably, NHA cells treated with Redox EVs exhibited 0.26 µM of H_2O_2

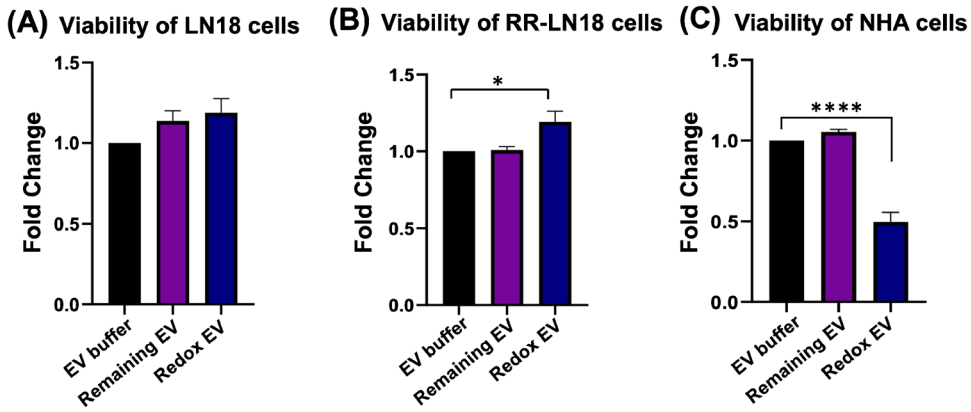

Fig. 7 Treatment of glioblastoma cells LN18, radiation resistance glioblastoma LN18 (RR-LN18), and normal human astrocytes (NHA cells) with Redox EVs show contrasting trends in cell viability. Cell viability using PrestoBlue was performed after EV treatments. **A** LN18 cells. **B** RR-LN18 cells, **C** NHA cells (*P<0.05) (****P<0.0001)

production, despite no detectable levels of H_2O_2 production at steady state (vehicle EV buffer treatment). This increase in H_2O_2 production correlated with the decrease in NHA cell viability, suggesting that Redox EVs induce NHA cell death through H_2O_2 overload. In contrast, Redox EVs induce GBM proliferation by promoting H_2O_2 production as signaling molecule. To further confirm that H_2O_2 contributing to cell viability of NHA cells and GBM cells, we further treated LN18 cells, RR-LN18 cells, and NHA cells, with 500 units of PEG-CAT, an enzyme that scavenges H_2O_2, for 24 h before administering

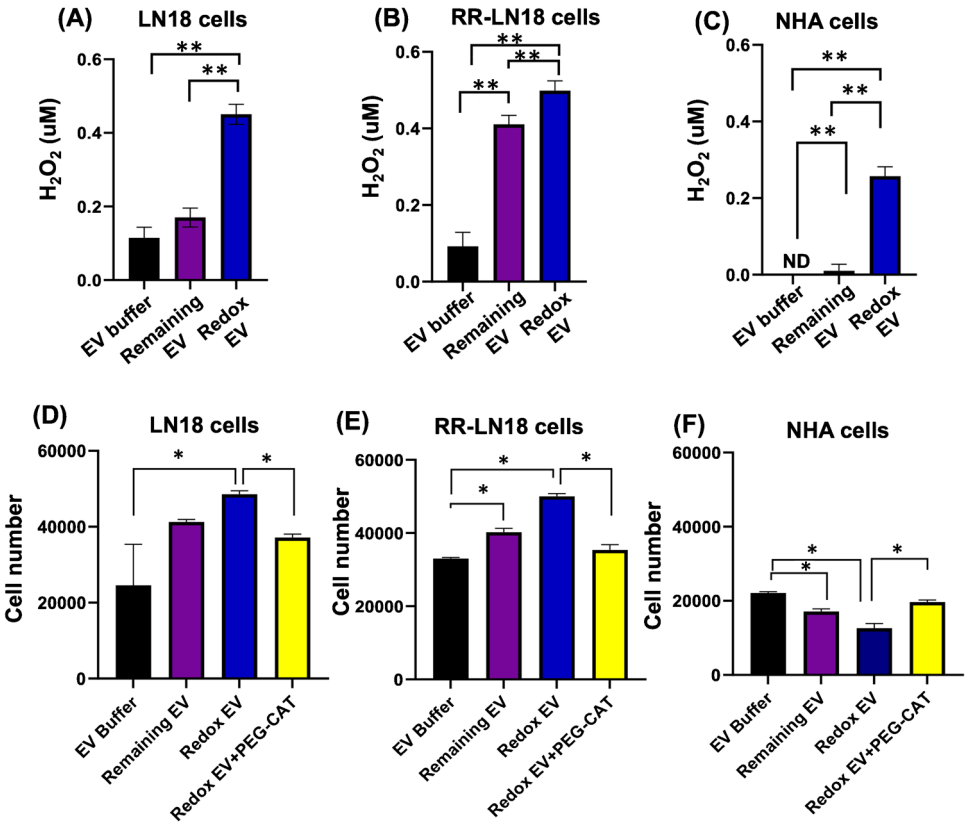

Fig. 8 Increased extracellular H_2O_2 production by Redox EVs in GBM and NHA cells are correlating to cell viability. Cells were treated with EV buffer (vehicle), Remaining EVs, or Redox EVs and incubated for 48 h before measuring H_2O_2 production using the Amplex Red assay. **A** LN18 cells, **B** RR-LN18 cells, and **C** NHA cells were analyzed. Compared with EV buffer and Remaining EVs, treatment with Redox EVs significantly increased extracellular H_2O_2 production in LN18 cells, RR-LN18 cells, and NHA cells. NHA cells produced detectable levels of H_2O_2 (0.26 μM), while RR-LN18 cells demonstrated the highest H_2O_2 production (0.5 μM). ND, non-detectable. **D–F** Cell number using Trypan blue were counted with hemocytometer after EV treatments. Polyethylene glycol catalase (PEG-CAT, 500 unit) were added to the cells 24 h prior to EV treatments to scavenge H_2O_2 production inside the cells. *P<0.05, **P<0.01 indicates statistically significant differences compared with controls

Remaining EVs or Redox EVs. Following treatments of EVs, we measured cell numbers using Trypan blue as described in the "Treatment with Redox EVs and cell viability of LN18 glioblastoma and normal human astrocyte cell lines" section. As shown in Fig. 8D–F, PEG-CAT pre-treatment significantly rescued NHA cells from the cytotoxic effects of Redox EVs, indicating a protective effect against H_2O_2-induced cell death. Moreover, in LN18 cells and RR-LN18 cells, PEG-CAT pre-treatment inhibited the cell growth that was otherwise promoted by Redox EVs. These data suggest that cancer-derived EVs that contain HNE (Redox EVs) are likely to be harmful to normal cells, while promoting cancer progression evinced by increased cell viability, at least in part by H_2O_2.

Even though, the treatment of irradiated GBM-derived EVs on both malignant and normal cells had varying effects, the impact on cancer cells' growth was minimal, but the impact on normal cells was drastic [59]. We postulate that the mechanism of Redox EVs uptaking on normal cells may contribute to such the differences. EVs shed from the plasma membrane often expose PtdSer [60]. Redox EVs expelled into the extracellular space are likely to have higher levels of PtdSer on the outer leaflet, enabling their uptake by surrounding cells through the TIM4 receptor [61]. NHA cells were observed to express higher levels of TIM4 receptor, thus facilitating increased uptake of Redox EVs which could resulting in higher H_2O_2 production in NHA cells, compared with GBM cells which have lower level of TIM4 receptor. Together, our findings suggest that the cargo released by Redox EVs into the cytosol of recipient cells has the potential to induce cell signaling pathways, including the upregulation of ROS production in the form of H_2O_2.

Conclusion

EVs have emerged as a biologic moiety and a platform for the use of liquid biopsy. Every normal and pathological cell can release EVs into the circulation, and different molecules encased within the EVs can be identifiers of features associated with the tissues from which they are derived. Due to the size and various subpopulations of EVs, selecting the appropriate isolation method that can effectively yield a wealth of EVs from small volume samples while also selecting for specific EVs populations. We recently identified that serum of GBM patients contain an abundant amount of EVs compared with serum from non-cancer individuals. More importantly, GBM-derived EVs contain a high level of 4 HNE-adducted proteins, both inside and on the surface of EVs (Redox EVs). However, current methods for isolating Redox EVs (e.g., flow cytometry sorting, immunoprecipitation) have limitations including being labor-intensive, high background noise, requirement for high volume of sample, and uncertainty regarding whether the EVs functionality can be assessed downstream (e.g., via irreversible binding of isolation reagents). Our study is the first to show that these limitations can be overcome by using the ESP technique. Further, we found that Redox EVs promote cell viability in GBM cells but kill normal astrocyte cells, via activation of H_2O_2 production. This finding could pave the way for understanding how cancers [62] and cancer treatments, i.e., radiation [29], which known to produce high levels of HNE, cause cognitive impairment in cancer patients, particularly cancers with high ROS levels. Establishing role(s) of GBM-derived Redox EVs in cognitive impairment will further highlight the novelty of exploiting EVs as a cancer stimulator or marker for neuronal injury. In summary, our study established and quantified, for the first time, the ability of ESP technology to isolate Redox EVs. The ESP technology provides an ideal experimental context to isolate Redox EVs and study the impact of Redox EVs on cognitive impairment, all of which is expected to have a broad translational application to other types of disease that are releasing EVs.

Supplementary Information The online version contains supplementary material available at https://doi.org/10.1007/s00216-024-05518-z.

Author contributions M.D.B., N.R.: Writing—original draft. D.A.B., D.S., S.M.B., L.C.: Writing—review and editing. M.D.B., N.R., J.M.C., S.B.: Investigation. M.D.B., N.R., J.M.C., S.B., N.R.,W.Z., K.M.: Methodology. M.D.B., N.R.: Validation. M.D.B., N.R.,W.Z., K.M.: Formal analysis. M.D.B., N.R., and L.C.: Visualization. S.M.B and L.C.: Conceptualization. D.A.B., D.S., S.M.B., L.C.: Project administration. S.M.B., L.C.: Supervision. S.M.B., L.C.: Funding acquisition.

Funding This work was supported, in part, by (1) NIH grants R01 CA251663 (L.C.), P20 GM148326 (L.C.), and R01 CA217934 (D.A.B. and D.S.) and (2) pilot funding to L.C and S.M.B. by Markey Cancer Center support grant (P30 CA177558). S.M.B., M.D.B., and S.B. were supported by NIH grants 1U01DA053903-01 and P30 ES026529, CDC contract BAA 75D301-20-R-68024, and NSF grant 2154934. The content is solely the responsibility of the authors and does not necessarily represent the official views of the National Institutes of Health.

Declarations

Competing interests The authors declare the following competing financial interest: Scott Berry has an ownership interest in Salus Discovery, LLC, which has licensed the ESP technology described in the text. All other authors declare no conflict of interest.

References

1. Möller A, Lobb RJ. The evolving translational potential of small extracellular vesicles in cancer. Nat Rev Cancer. 2020;20:697–709. https://doi.org/10.1038/s41568-020-00299-w.
2. Miller CE, Xu F, Zhao Y, Luo W, Zhong W, Meyer K, et al. Hydrogen peroxide promotes the production of radiation-derived EVs containing mitochondrial proteins. Antioxidants. 2022;11:2119. https://doi.org/10.3390/antiox11112119.
3. Kinoshita T, Yip KW, Spence T, Liu F-F. MicroRNAs in extracellular vesicles: potential cancer biomarkers. J Hum Genet. 2017;62:67–74. https://doi.org/10.1038/jhg.2016.87.

4. Greening DW, Xu R, Ji H, Tauro BJ, Simpson RJ. A protocol for exosome isolation and characterization: evaluation of ultracentrifugation, density-gradient separation, and immunoaffinity capture methods, 2015, p. 179–209. https://doi.org/10.1007/978-1-4939-2550-6_15.
5. Havers M, Broman A, Lenshof A, Laurell T. Advancement and obstacles in microfluidics-based isolation of extracellular vesicles. Anal Bioanal Chem. 2023;415:1265–85. https://doi.org/10.1007/s00216-022-04362-3.
6. Nguyen A, Turko IV. Isolation protocols and mitochondrial content for plasma extracellular vesicles. Anal Bioanal Chem. 2023;415:1299–304. https://doi.org/10.1007/s00216-022-04465-x.
7. Oliveira-Rodríguez M, López-Cobo S, Reyburn HT, Costa-García A, López-Martín S, Yáñez-Mó M, et al. Development of a rapid lateral flow immunoassay test for detection of exosomes previously enriched from cell culture medium and body fluids. J Extracell Vesicles. 2016;5:31803. https://doi.org/10.3402/jev.v5.31803.
8. Sharma P, Ludwig S, Muller L, Hong CS, Kirkwood JM, Ferrone S, et al. Immunoaffinity-based isolation of melanoma cell-derived exosomes from plasma of patients with melanoma. J Extracell Vesicles. 2018;7:1435138. https://doi.org/10.1080/20013078.2018.1435138.
9. Yoshioka Y, Kosaka N, Konishi Y, Ohta H, Okamoto H, Sonoda H, et al. Ultra-sensitive liquid biopsy of circulating extracellular vesicles using ExoScreen. Nat Commun. 2014;5:3591. https://doi.org/10.1038/ncomms4591.
10. Fang S, Tian H, Li X, Jin D, Li X, Kong J, et al. Clinical application of a microfluidic chip for immunocapture and quantification of circulating exosomes to assist breast cancer diagnosis and molecular classification. PLoS One. 2017;12:e0175050. https://doi.org/10.1371/journal.pone.0175050.
11. Zhang P, He M, Zeng Y. Ultrasensitive microfluidic analysis of circulating exosomes using a nanostructured graphene oxide/polydopamine coating. Lab Chip. 2016;16:3033–42. https://doi.org/10.1039/C6LC00279J.
12. Ni F, Zhu Q, Li H, Liu F, Chen H. Efficient preparation of high-purity and intact mesenchymal stem cell–derived extracellular vesicles. Anal Bioanal Chem. 2024;416:1797–808. https://doi.org/10.1007/s00216-024-05193-0.
13. Ströhle G, Gan J, Li H. Affinity-based isolation of extracellular vesicles and the effects on downstream molecular analysis. Anal Bioanal Chem. 2022;414:7051–67. https://doi.org/10.1007/s00216-022-04178-1.
14. Sato H, Shibata M, Shimizu T, Shibata S, Toriumi H, Ebine T, et al. Differential cellular localization of antioxidant enzymes in the trigeminal ganglion. Neuroscience. 2013;248:345–58. https://doi.org/10.1016/j.neuroscience.2013.06.010.
15. Pizzino G, Irrera N, Cucinotta M, Pallio G, Mannino F, Arcoraci V, et al. Oxidative stress: harms and benefits for human health. Oxid Med Cell Longev. 2017;2017:1–13. https://doi.org/10.1155/2017/8416763.
16. Dalleau S, Baradat M, Guéraud F, Huc L. Cell death and diseases related to oxidative stress:4-hydroxynonenal (HNE) in the balance. Cell Death Differ. 2013;20:1615–30. https://doi.org/10.1038/cdd.2013.138.
17. Chiarpotto* E, Domenicotti* C, Paola D, Vitali A, Nitti M, Pronzato MA, et al. Regulation of rat hepatocyte protein kinase C ? isoenzymes by the lipid peroxidation product 4-hydroxy-2,3-nonenal: a signaling pathway to modulate vesicular transport of glycoproteins. Hepatology 1999;29:1565–72. https://doi.org/10.1002/hep.510290510.
18. Uchida K, Toyokuni S, Nishikawa K, Kawakishi S, Oda H, Hiai H, et al. Michael addition-type 4-hydroxy-2-nonenal adducts in modified low-density lipoproteins: markers for atherosclerosis. Biochemistry. 1994;33:12487–94. https://doi.org/10.1021/bi00207a016.
19. Poli G, Schaur RJ, Siems WG, Leonarduzzi G. 4-Hydroxynonenal: a membrane lipid oxidation product of medicinal interest. Med Res Rev. 2008;28:569–631. https://doi.org/10.1002/med.20117.
20. Subramaniam R, Roediger F, Jordan B, Mattson MP, Keller JN, Waeg G, et al. The lipid peroxidation product, 4-hydroxy-2-trans-nonenal, alters the conformation of cortical synaptosomal membrane proteins. J Neurochem. 2002;69:1161–9. https://doi.org/10.1046/j.1471-4159.1997.69031161.x.
21. Butterfield DA, Halliwell B. Oxidative stress, dysfunctional glucose metabolism and Alzheimer disease. Nat Rev Neurosci. 2019;20:148–60. https://doi.org/10.1038/s41583-019-0132-6.
22. Barrera G. Oxidative stress and lipid peroxidation products in cancer progression and therapy. ISRN Oncol. 2012;2012:1–21. https://doi.org/10.5402/2012/137289.
23. Bader Lange ML, Cenini G, Piroddi M, Mohmmad Abdul H, Sultana R, Galli F, et al. Loss of phospholipid asymmetry and elevated brain apoptotic protein levels in subjects with amnestic mild cognitive impairment and Alzheimer disease. Neurobiol Dis. 2008;29:456–64. https://doi.org/10.1016/j.nbd.2007.11.004.
24. Firl N, Kienberger H, Hauser T, Rychlik M. Determination of the fatty acid profile of neutral lipids, free fatty acids and phospholipids in human plasma. Clinical Chemistry and Laboratory Medicine (CCLM). 2013;51:799–810. https://doi.org/10.1515/cclm-2012-0203.
25. Morel O, Jesel L, Freyssinet J-M, Toti F. Cellular mechanisms underlying the formation of circulating microparticles. Arterioscler Thromb Vasc Biol. 2011;31:15–26. https://doi.org/10.1161/ATVBAHA.109.200956.
26. Ho J, Chaiswing L, Clair DK. Extracellular vesicles and cancer therapy: insights into the role of oxidative stress. Antioxidants. 2022;11:1194. https://doi.org/10.3390/antiox11061194.
27. Zhang S, Eitan E, Wu T-Y, Mattson MP. Intercellular transfer of pathogenic α-synuclein by extracellular vesicles is induced by the lipid peroxidation product 4-hydroxynonenal. Neurobiol Aging. 2018;61:52–65. https://doi.org/10.1016/j.neurobiolaging.2017.09.016.
28. Szweda LI, Uchida K, Tsai L, Stadtman ER. Inactivation of glucose-6-phosphate dehydrogenase by 4-hydroxy-2-nonenal. Selective modification of an active-site lysine. J Biol Chem. 1993;268:3342–7.
29. Sukati S, Ho J, Chaiswing L, Sompol P, Pandit H, Wei W, et al. Extracellular vesicles released after cranial radiation: an insight into an early mechanism of brain injury. Brain Res. 2022;1782:147840. https://doi.org/10.1016/j.brainres.2022.147840.
30. Rummel NG, Chaiswing L, Bondada S, Clair DK, Butterfield DA. Chemotherapy-induced cognitive impairment: focus on the intersection of oxidative stress and TNFα. Cell Molecular Life Sci. 2021;78:6533–40. https://doi.org/10.1007/s00018-021-03925-4.
31. Malloci M, Perdomo L, Veerasamy M, Andriantsitohaina R, Simard G, Martínez MC. Extracellular vesicles: mechanisms in human health and disease. Antioxid Redox Signal. 2019;30:813–56. https://doi.org/10.1089/ars.2017.7265.
32. Ricklefs FL, Wollmann K, Salviano-Silva A, Drexler R, Maire CL, Kaul MG, et al. Circulating extracellular vesicles as biomarker for diagnosis, prognosis, and monitoring in glioblastoma patients. Neuro Oncol. 2024;26:1280–91. https://doi.org/10.1093/neuonc/noae068.
33. Osti D, Del Bene M, Rappa G, Santos M, Matafora V, Richichi C, et al. Clinical significance of extracellular vesicles in plasma from glioblastoma patients. Clin Cancer Res. 2019;25:266–76. https://doi.org/10.1158/1078-0432.CCR-18-1941.
34. Sidhom K, Obi PO, Saleem A. A review of exosomal isolation methods: is size exclusion chromatography the best option? Int

J Mol Sci. 2020;21:6466. https://doi.org/10.3390/ijms21186466.
35. De Sousa KP, Rossi I, Abdullahi M, Ramirez MI, Stratton D, Inal JM. Isolation and characterization of extracellular vesicles and future directions in diagnosis and therapy. WIREs Nanomed Nanobiotechnol. 2023;15:e1835. https://doi.org/10.1002/wnan.1835.
36. Morales-Kastresana A, Musich TA, Welsh JA, Telford W, Demberg T, Wood JCS, et al. High-fidelity detection and sorting of nanoscale vesicles in viral disease and cancer. J Extracell Vesicles. 2019;8:1597603. https://doi.org/10.1080/20013078.2019.1597603.
37. Berry SM, Chin EN, Jackson SS, Strotman LN, Goel M, Thompson NE, et al. Weak protein–protein interactions revealed by immiscible filtration assisted by surface tension. Anal Biochem. 2014;447:133–40. https://doi.org/10.1016/j.ab.2013.10.038.
38. Casavant BP, Guckenberger DJ, Beebe DJ, Berry SM. Efficient sample preparation from complex biological samples using a sliding lid for immobilized droplet extractions. Anal Chem. 2014;86:6355–62. https://doi.org/10.1021/ac500574t.
39. Berry SM, Pezzi HM, Williams ED, Loeb JM, Guckenberger DJ, Lavanway AJ, et al. Using exclusion-based sample preparation (ESP) to reduce viral load assay cost. PLoS One. 2015;10:e0143631. https://doi.org/10.1371/journal.pone.0143631.
40. Sperger JM, Strotman LN, Welsh A, Casavant BP, Chalmers Z, Horn S, et al. Integrated analysis of multiple biomarkers from circulating tumor cells enabled by exclusion-based analyte isolation. Clin Cancer Res. 2017;23:746–56. https://doi.org/10.1158/1078-0432.CCR-16-1021.
41. Strike W, Amirsoleimani A, Olaleye A, Noble A, Lewis K, Faulkner L, et al. Development and validation of a simplified method for analysis of SARS-CoV-2 RNA in University Dormitories. ACS ES&T Water. 2022;2:1984–91. https://doi.org/10.1021/acsestwater.2c00044.
42. Torabi S, Amirsoleimani A, DehghanBanadaki M, Strike WD, Rockward A, Noble A, et al. Stabilization of SARS-CoV-2 RNA in wastewater via rapid RNA extraction. Sci Total Environ. 2023;878: 162992. https://doi.org/10.1016/j.scitotenv.2023.162992.
43. DehghanBanadaki M, Torabi S, Rockward A, Strike WD, Noble A, Keck JW, et al. Simple SARS-CoV-2 concentration methods for wastewater surveillance in low resource settings. Sci Total Environ. 2024;912: 168782. https://doi.org/10.1016/j.scitotenv.2023.168782.
44. Moussavi-Harami SF, Annis DS, Ma W, Berry SM, Coughlin EE, Strotman LN, et al. Characterization of molecules binding to the 70K N-terminal region of fibronectin by IFAST purification coupled with mass spectrometry. J Proteome Res. 2013;12:3393–404. https://doi.org/10.1021/pr400225p.
45. Goel S, Chin EN, Fakhraldeen SA, Berry SM, Beebe DJ, Alexander CM. Both LRP5 and LRP6 receptors are required to respond to physiological Wnt ligands in mammary epithelial cells and fibroblasts. J Biol Chem. 2012;287:16454–66. https://doi.org/10.1074/jbc.M112.362137.
46. DehghanBanadaki M, Torabi S, Strike WD, Noble A, Keck JW, Berry SM. Improving wastewater-based epidemiology performance through streamlined automation. J Environ Chem Eng. 2023;11: 109595. https://doi.org/10.1016/j.jece.2023.109595.
47. Nguyen U, Squaglia N, Boge A, Fung PA. The simple Western™: a gel-free, blot-free, hands-free Western blotting reinvention. Nat Methods. 2011;8:v–vi. https://doi.org/10.1038/nmeth.f.353.
48. Hill JL, McIver KB, Katzer K, Foster MT. Capillary western immunoassay optimization of estrogen related factors in human subcutaneous adipose tissue. Methods Protoc. 2022;5:34. https://doi.org/10.3390/mps5020034.
49. Becker A, Thakur BK, Weiss JM, Kim HS, Peinado H, Lyden D. Extracellular vesicles in cancer: cell-to-cell mediators of metastasis. Cancer Cell. 2016;30:836–48. https://doi.org/10.1016/j.ccell.2016.10.009.
50. Chiaradia E, Tancini B, Emiliani C, Delo F, Pellegrino RM, Tognoloni A, et al. Extracellular vesicles under oxidative stress conditions: biological properties and physiological roles. Cells. 2021;10:1763. https://doi.org/10.3390/cells10071763.
51. Kim W, Lee S, Seo D, Kim D, Kim K, Kim E, et al. Cellular stress responses in radiotherapy. Cells. 2019;8:1105. https://doi.org/10.3390/cells8091105.
52. Chaiswing L, Weiss HL, Jayswal RD, Clair DK, Kyprianou N. Profiles of radioresistance mechanisms in prostate cancer. Crit Rev Oncog. 2018;23:39–67. https://doi.org/10.1615/CritRevOncog.2018025946.
53. Matsumura S, Minamisawa T, Suga K, Kishita H, Akagi T, Ichiki T, et al. Subtypes of tumour cell-derived small extracellular vesicles having differently externalized phosphatidylserine. J Extracell Vesicles. 2019;8:1579541. https://doi.org/10.1080/20013078.2019.1579541.
54. Nagata S, Suzuki J, Segawa K, Fujii T. Exposure of phosphatidylserine on the cell surface. Cell Death Differ. 2016;23:952–61. https://doi.org/10.1038/cdd.2016.7.
55. Welsh JA, Goberdhan DCI, O'Driscoll L, Buzas EI, Blenkiron C, Bussolati B, et al. Minimal information for studies of extracellular vesicles (MISEV2023): from basic to advanced approaches. J Extracell Vesicles. 2024;13: e12404. https://doi.org/10.1002/jev2.12404.
56. Saha B, Evers TH, Prins MWJ. How antibody surface coverage on nanoparticles determines the activity and kinetics of antigen capturing for biosensing. Anal Chem. 2014;86:8158–66. https://doi.org/10.1021/ac501536z.
57. Lennicke C, Rahn J, Lichtenfels R, Wessjohann LA, Seliger B. Hydrogen peroxide – production, fate and role in redox signaling of tumor cells. Cell Communication Signal. 2015;13:39. https://doi.org/10.1186/s12964-015-0118-6.
58. Park I, Hwang J, Kim YM, Ha J, Park OJ. Differential modulation of AMPK signaling pathways by low or high levels of exogenous reactive oxygen species in colon cancer cells. Ann N Y Acad Sci. 2006;1091:102–9. https://doi.org/10.1196/annals.1378.059.
59. Borovic S, Cipak A, Meinitzer A, Kejla Z, Perovic D, Waeg G, et al. Differential sensitivity to 4-hydroxynonenal for normal and malignant mesenchymal cells. Redox Rep. 2007;12:50–4. https://doi.org/10.1179/135100007X162194.
60. Wei H, Malcor J-DM, Harper MT. Lipid rafts are essential for release of phosphatidylserine-exposing extracellular vesicles from platelets. Sci Rep 2018;8:9987. https://doi.org/10.1038/s41598-018-28363-4.
61. Flannagan RS, Canton J, Furuya W, Glogauer M, Grinstein S. The phosphatidylserine receptor TIM4 utilizes integrins as coreceptors to effect phagocytosis. Mol Biol Cell. 2014;25:1511–22. https://doi.org/10.1091/mbc.e13-04-0212.
62. Zhong H, Yin H. Role of lipid peroxidation derived 4-hydroxynonenal (4-HNE) in cancer: focusing on mitochondria. Redox Biol. 2015;4:193–9. https://doi.org/10.1016/j.redox.2014.12.011.